Published online 20 November 2018 *Nucleic Acids Research, 2019, Vol. 47, No. 3* **1225–1238**
doi: 10.1093/nar/gky1192

Direct interaction between the PRDM3 and PRDM16 tumor suppressors and the NuRD chromatin remodeling complex

Danton Ivanochko[1,2,3], Levon Halabelian[3], Elizabeth Henderson[4], Pavel Savitsky[4], Harshika Jain[3], Edyta Marcon[5,6], Shili Duan[2], Ashley Hutchinson[3], Alma Seitova[3], Dalia Barsyte-Lovejoy[3], Panagis Filippakopoulos[4], Jack Greenblatt[5,6], Evelyne Lima-Fernandes[1,2,3,*] and Cheryl H. Arrowsmith[1,2,3,*]

[1]Department of Medical Biophysics, University of Toronto, Toronto, ON, M5G 1L7, Canada, [2]Princess Margaret Cancer Centre, University Health Network, Toronto, ON, M5G 2M9, Canada, [3]Structural Genomics Consortium, University of Toronto, Toronto, ON, M5G 1L7, Canada, [4]Structural Genomics Consortium, Nuffield Department of Clinical Medicine, University of Oxford, Oxford, OX3 7DQ, United Kingdom, [5]Department of Molecular Genetics, University of Toronto, Toronto, ON, M5S 1A8, Canada and [6]Donnelly Centre for Cellular and Biomolecular Research, University of Toronto, Toronto, ON, M5S 3E1, Canada

Received August 02, 2018; Revised October 31, 2018; Editorial Decision November 08, 2018; Accepted November 15, 2018

ABSTRACT

Aberrant isoform expression of chromatin-associated proteins can induce epigenetic programs related to disease. The MDS1 and EVI1 complex locus (*MECOM*) encodes PRDM3, a protein with an N-terminal PR-SET domain, as well as a shorter isoform, EVI1, lacking the N-terminus containing the PR-SET domain (ΔPR). Imbalanced expression of MECOM isoforms is observed in multiple malignancies, implicating EVI1 as an oncogene, while PRDM3 has been suggested to function as a tumor suppressor through an unknown mechanism. To elucidate functional characteristics of these N-terminal residues, we compared the protein interactomes of the full-length and ΔPR isoforms of PRDM3 and its closely related paralog, PRDM16. Unlike the ΔPR isoforms, both full-length isoforms exhibited a significantly enriched association with components of the NuRD chromatin remodeling complex, especially RBBP4. Typically, RBBP4 facilitates chromatin association of the NuRD complex by binding to histone H3 tails. We show that RBBP4 binds to the N-terminal amino acid residues of PRDM3 and PRDM16, with a dissociation constant of 3.0 μM, as measured by isothermal titration calorimetry. Furthermore, high-resolution X-ray crystal structures of PRDM3 and PRDM16 N-terminal peptides in complex with RBBP4 revealed binding to RBBP4 within the conserved histone H3-binding groove. These data support a mechanism of isoform-specific interaction of PRDM3 and PRDM16 with the NuRD chromatin remodeling complex.

INTRODUCTION

The MDS1 and EVI1 complex locus (*MECOM*) encodes two isoform subgroups through the induction of alternate transcription start sites preceding either MDS1 or EVI1 loci (1). Either the *MECOM*-encompassing PRDM3 isoforms or the MDS1-lacking EVI1 isoforms can be produced, with additional isoforms arising from alternative splicing events. PRDM3 belongs to the PRDM family of transcription factors characterized by an N-terminal PR-SET domain, followed by an array of C2H2 zinc finger motifs, while EVI1 possesses the zinc fingers but is N-terminally truncated and lacks the PR-SET domain (ΔPR). PRDM16 (also known as MEL1) is a closely related paralog of PRDM3 sharing 53% sequence identity with the N-terminus of PRDM3, which can also be omitted through expression of the ΔPR PRDM16 isoform (2).

MECOM and *PRDM16* gene expression has been observed across many tissue types and both are implicated in haematopoietic development (3,4). The PRDM3 isoform is critical for maintaining long-term hematopoietic stem cell function, while the EVI1 isoform has an essential role in hematopoiesis. However, *MECOM* expression declines after hematopoiesis (5). PRDM16 is preferentially expressed

*To whom correspondence should be addressed. Tel: +1 416 946 0881; Fax: +1 416 946 0880; Email: Cheryl.Arrowsmith@uhnresearch.ca
Correspondence may also be addressed to Evelyne Lima-Fernandes. Tel: +1 416 581 8550 (Ext. 7558); Fax: +1 416 634 7200; Email: evelyne.lima.fernandes@utoronto.ca

© The Author(s) 2018. Published by Oxford University Press on behalf of Nucleic Acids Research.
This is an Open Access article distributed under the terms of the Creative Commons Attribution Non-Commercial License (http://creativecommons.org/licenses/by-nc/4.0/), which permits non-commercial re-use, distribution, and reproduction in any medium, provided the original work is properly cited. For commercial re-use, please contact journals.permissions@oup.com

by haematopoietic and neuronal stem cells and functions to attenuate reactive oxygen species-related stress through the promotion of hepatocyte growth factor gene expression (6,7). Additionally, PRDM16 is a key determinant of brown adipose tissue identity by suppressing genes of white adipose tissue, while independently activating genes for brown adipose tissue (8–10). Proteins that drive key developmental pathways are frequently dysregulated in cancer and thus it is no surprise that both PRDM3 and PRDM16 are directly linked to various aspects of oncogenic transformation.

A Yin-Yang analogy describes the isoform imbalance observed with some PRDM proteins that either function as tumor suppressors or oncogenes depending on the retention of the PR-SET domain (11). For example, EVI1 is a potent oncogene associated with transformation and proliferation in multiple leukemias, while expression of PRDM3 is frequently abrogated and a low PRDM3/EVI1 expression ratio predicts an extremely poor prognosis for acute myeloid leukemia (AML) patients (1,12–15). Additionally, in solid tumors from ovarian and hepatocellular carcinomas, EVI1 overexpression has been shown to drive oncogenesis and progression, while EVI1 in colon cancer was shown to be critical for metastasis (16–18). Aberrant *MECOM* isoform expression can arise from 3q26 genomic rearrangements imparting an imbalance between EVI1 and PRDM3 isoforms and with it, poor patient survival in AML (15,19). Rearrangements may arise from retroviral insertions between the MDS1 and EVI1 loci, which interrupt normal PRDM3 transcription and lead to EVI1 overexpression (12,20,21). Some leukemia patients lack an altered 3q26 karyotype and instead overexpress the EVI1 isoform through activation by mixed-lineage leukemia (MLL) chimeric genes MLL-ENL or MLL-AF9 (22). *PRDM16* is similar to the *MECOM* gene, wherein lentiviral-induced genomic alterations lead to depletion of full-length PRDM16 and higher levels of the N-terminally truncated ΔPR PRDM16 isoform, while full-length PRDM16 may also function as a tumor suppressor protein in leukemias (2,21,23–25). Together, these consistent pathologies, along with the high sequence conservation between the PRDM3 and PRDM16 proteins, appear to suggest that an exclusive molecular property of both full-length isoforms can function to repress certain aspects of tumor formation and/or progression.

The N-terminal PR-SET domain belongs to a distinct class of SET domains that are sometimes described for a lack of intrinsic lysine methyltransferase (KMT) activity. Reported KMT activity for PRDM3 and PRDM16 PR-SET domains includes weak mono-methyltransferase activity on lysine 9 of histone H3 (H3K9me1), which occurs in the cytosol (26). Additionally, PRDM16 has been reported to methylate lysine 9 and lysine 4 on histone H3 in separate studies (25,27). Interestingly, a key catalytic tyrosine residue present in the robustly active KMT enzyme PRDM9, as well as in all other demonstrably enzymatic SET domains, is absent from PRDM3 and PRDM16, suggesting a potential alternative function of these N-terminal domains (28,29). The C-terminal zinc finger motifs of PRDM3 and PRDM16 cluster into two separate domains and facilitate specific interactions with DNA. In PRDM3, the N-terminal zinc fingers bind a GATA-like motif and the C-terminal zinc fingers bind to an ETS-like motif (30,31). ChIP-seq analysis of EVI1-binding sites in SKOV3 ovarian carcinoma cells demonstrated enrichment at myeloid leukemia genes (32), while an analysis across a panel of AML cell lines found that EVI1 binding leads to deregulation of genes involved in apoptosis, differentiation and proliferation (33). Interestingly, while PRDM16 can localize to the same DNA-binding sites as PRDM3/EVI1 through its zinc finger domains, ChIP-seq analysis suggests that PRDM16 can be recruited indirectly to chromatin in brown adipose tissue via interactions with DNA-binding partners, including C/EBPβ and PPARγ, rather than by direct binding to DNA (10,23). Both PRDM3 and PRDM16 bind to C-terminal binding protein (CtBP) through canonical PLDLS CtBP-binding sites located between the two zinc finger clusters, which can promote cellular growth by repressing transcription downstream of transforming growth factor-β signaling (34,35). Additionally, the EVI1 isoform has been reported to form homo-oligomers capable of enhanced CtBP binding (36). While it is well established that the zinc finger motifs direct genomic localization, it remains unclear if the N-terminal amino acids that are exclusive to full-length PRDM3 and PRDM16 contribute to biologically relevant protein–protein interactions.

The NuRD chromatin remodeling complex is an essential epigenetic regulator of developmental genes. In haematopoietic stem cells, NuRD regulates the expression of genetic pathways critical for proliferation and differentiation, while perturbation of NuRD signaling is associated with cancer and premature aging (37). The NuRD complex possesses adenosine triphosphate-dependent chromatin-remodeling and histone deacetylase activities conferred by CHD3 and CHD4 (chromodomain/helicase/DNA-binding) proteins and HDAC1 and HDAC2 (histone deacetylase) proteins, respectively (38). Structural studies suggest that the core NuRD complex contains the HDAC1 and HDAC2 proteins, the MTA1 and MTA2 (metastasis-associated) proteins, as well as the RBBP4 and RBBP7 proteins (38,39). Additional complex members include the CHD3 and CHD4 proteins, the MBD2 and MBD3 (methyl-CpG-binding domain) proteins and the GATAD2A and GATAD2B (GATA Zinc Finger Domain Containing) proteins (38). The NuRD complex is composed of multiple RBBP4/7 subunits, which scaffold between histone H3 tails and MTA1/2 subunits. (38–40). Several transcription factors are known to bind RBBP4/7 in the NuRD complex by competing for the histone H3 binding interface, including SALL1, FOG1, PHF6 and BCL11A (41–44). Interestingly, FOG1 forms a strong interaction with RBBP4 and has a secondary interaction with the MTA proteins within the NuRD complex (42,45). A previous immunoprecipitation with mass spectrometry (IP-MS) screen of EVI1 interactions has identified the NuRD complex members RBBP4, HDAC1, HDAC2 and CHD4 as potential interactors (46). Additionally, a yeast two-hybrid screen found that EVI1 interacts with the MBD3b protein (47), but this interaction was not observed in IP-MS assay (46). It remains unclear how EVI1 interacts with the NuRD complex and whether the N-terminal residues of PRDM3 contribute to these interactions.

In this study, we find that the RNA expression profiles of *MECOM* transcripts across a panel of solid tumors sup-

port the Yin-Yang hypothesis of a cancer-specific imbalance of full-length PRDM3 and the ΔPR isoform known as EVI1. Using proteomics IP-MS experiments to compare the interactomes of the full-length and ΔPR isoforms of PRDM3 and PRDM16, we determine that NuRD complex members are significantly enriched for both full-length proteins compared to the ΔPR counterparts. Through biophysical characterization and cellular co-localization analysis, we identify an interaction between the N-terminal residues of full-length PRDM3 and PRDM16 with RBBP4 and present the crystal structures of PRDM3 and PRDM16 peptides (residues 1–12) bound to RBBP4 perpendicular to the electronegative β-propeller axis typically occupied by the histone H3 tail. Together, these data provide a molecular and structural framework for understanding how full-length PRDM3 and PRDM16 may regulate epigenetic machinery which is lost in some cancers.

MATERIALS AND METHODS

Gene and isoform expression analysis

The Cancer Genome Atlas (TCGA) datasets for *MECOM* transcript expressions were obtained from the FireBrowse resource (http://firebrowse.org/), for all patients with matched healthy and tumor tissue samples (Supplementary Table S1). *MECOM* gene expression was estimated from the summation of RSEM normalized counts for each transcript and statistical significance was calculated with the R programming language (version 3.2) (48). *MECOM* transcript expression levels from healthy and tumor samples from TCGA studies where *MECOM* expression was significantly decreased was used to perform a principal component analysis (PCA) using the 'prcom' function in the R environment.

Co-Immunoprecipitation and mass spectroscopy

T47D cells were transfected with GFP-tagged, murine Prdm3 or Prdm16 plasmids using Turbofect following manufacturer's recommendations. Forty eight hours after transfection, cells were washed with ice-cold phosphate buffered saline (PBS), and lysed in high-salt buffer (10 mM Tris–HCl, pH 7.9, 420 mM NaCl, 0.1% NP-40), followed by three freeze–thaw cycles. After lysates were cleared by centrifugation (13 000 rpm for 20 min at 4°C), 5% of the lysates were saved for western blot input controls and 80% was used for the IP procedures.

For the immunoprecipitation step, the lysates were incubated with 5 μg of anti-GFP antibody (Invitrogen) overnight at 4°C. Magnetic protein A/G beads (Dynabeads, Life technologies), were mixed at 1:1 ratio (10 μl of each per sample) and washed with low salt AFC buffer twice (10 mM Tris–HCl, pH 7.9, 100 mM NaCl, 0.1% NP-40). The beads were incubated 4 h at 4°C with the lysate/antibody mix and washed twice in low-salt AFC. The beads were washed a 3rd time in low-salt AFC in the absence of NP-4 and eluted in 0.5 M ammonium hydroxide, before flash freezing in liquid nitrogen.

For the MS procedure, samples were dried in a Speedvac concentrator (Eppendorf) and reconstituted in 44 μl of 50 mM NH4HCO3 and 1 μl of 100 mM tris(2-carboxyethyl)phosphine, pH 7.5 (TCEP-HCl). Samples were incubated at 37°C for 1 h with shaking and cooled down to room temperature before adding 1 μl 500 mM iodoacetamide. Samples were incubated in the dark at room temperature for 45 min, then digested using 1 μg Trypsin (Promega) with overnight incubation at 37°C, and the reaction was stopped with 2 μl of acetic acid. Samples were desalted using Zip-Tips (Millipore) following the manufacturer's instructions and processed for MS using an Orbitrap Velos mass spectrometer (Thermo Fisher Scientific).

co-IP validation experiment and western blot

For co-IP experiment on transfected T74D cells, cell lysis and immunoprecipitation were performed as described in the IP-MS experiment, except for the third wash and elution. The beads were washed a third time in low salt AFC, resuspended in 30 μl of Laemmli buffer and boiled for 5 min. The whole 30 μl were processed for western blot using antibodies for GFP (Living Colors JL-8, Clontech), RBBP4 (R&D systems, MAB7416-SP), MTA1 (CST, 5647) and HDAC2 (CST, 5113). Endogenous co-IP experiments were performed on T47D and MCF7 cells using the same methodology as described above, using 5 μg of RBBP4 antibody (Abcam, ab79416) for the IP and blotted with PRDM3/EVI1antibody (ab124934).

Mass Spectrometry analysis

SAINTexpress (v3.6.1) (49) was used to calculate the probability that identified proteins from the Immunoprecipitation and mass spectroscopy experiments were significantly enriched above background contaminants by comparing the expected and observed peptide counts between the GFP-tagged prey proteins and the GFP-only negative control ($n = 3$). Prey proteins with a calculated Bayesian false discovery rate of ≤1% where called as high confidence protein–protein interactions (Supplementary Table S1) and sorted by odds ratio for each bait–prey interaction with the full-length and ΔPR isoforms.

Cellular co-localization analysis

Full-length mouse Prdm3 complementary DNA (cDNA) (National Center for Biotechnology Information (NCBI) accession number NM_001361034) or a truncated mutant lacking the first twelve amino-acids were amplified by polymerase chain reaction (PCR) and cloned into the AgeI site of the mCherry-LacR-NLS-KpnI plasmid (Luijsterburg *et al.*, 2012) to generate a C-terminally fused mCherry-LacR-NLS tag onto Prdm3. Full-length human RBBP4 cDNA (NCBI accession number NM_005610) was amplified by PCR and cloned into pDONR221 vector with Gateway BP Clonase II mix and then transferred into the pCDNA6.2/N-EmGFP-DEST vector with Gateway LR Clonase II mix (ThermoFisher Scientific). Constructs encoding an N-terminal mCherry-LacR-NLS tag onto Prdm3 were cloned into the KpnI site of the same vector. All constructs were verified by sequencing.

U-2 OS cells expressing 256 repeats of a LacO array (U-2 OS LacO Cells, previously described (50)) were cultured in

DMEM media (Thermo Fisher Scientific, cat. #31966021) supplemented with 10% fetal bovine serum (v/v, Biosera, cat. #FB-1001/500) and antibiotics (1% Pencillin Streptomycin (Thermo Fisher Scientific, cat. #15070063), 1 μg/ml puromycin (Thermo Fisher Scientific, cat. #A1113803) at 37°C and 10% CO_2.

U-2 OS LacO cells were washed with PBS, trypsinized using 0.25% trypsin-ethylenediaminetetraacetic acid(Thermo Fisher Scientific, cat. #25200056) for 3 min at room temperature and seeded in 24-well cell culture dishes (30 000 cells in 1 ml media per well). After incubating for 20 h at 37°C and 10% CO_2, cells were transfected with plasmids using the FuGENE6 reagent (Promega, cat #E2311) according to the manufacturer's instructions (100 ng per plasmid in 20 μl OptiMem (Thermo Fisher Scientific, cat. #31985070) with 1 μl FuGENE6 per well), then incubated for 24 h at 37°C and 10% CO_2. Transfected cells were then washed with PBS, trypsinized and re-plated onto 8-well glass imaging chamber dishes (Thermo Fisher Scientific, cat. #155411PK) in 300 μl media. Cells were incubated for 20–24 h at 37°C and 5% CO_2 before fixing.

Cells were washed with PBS twice before fixing at room temperature with 4% formaldehyde (300 μl in PBS) for 10 min, then washed twice with PBS, and were subsequently incubated with 0.2% Triton-X100 (300 μl in PBS) for 5 min at room temperature. Cells were washed with PBS three times, then incubated with a 4′,6-diamidino-2-phenylindole (DAPI) solution (300 μl of 1 μg/ml from a 1 mg/ml stock; Thermo Fisher Scientific, cat. #62248) for 2 min at room temperature. Cells were washed twice with PBS, and then glycerol buffer (300 μl, 90% glycerol, 10% 20 mM Tris–HCl pH 8.0) was added to the cells. Cells were stored at room temperature, away from light and were imaged within one week of fixing.

Cells were imaged using a Zeiss LSM 710 scan-head (Zeiss GmbH, Jena, Germany) coupled to an inverted Zeiss Axio Observer Z1 microscope equipped with a high-numerical-aperture (N. A. 1.40) 63 × oil immersion objective (Zeiss GmbH, Jena, Germany). A 488 nm excitation laser and a 494–542 nm emission filter were used to detect GFP fluorescence. A 594 nm excitation laser and a 598–700 nm emission filter were used to detect mCherry fluorescence. Quantification was carried out using the ImageJ software. Co-localization enrichment was calculated using the following formula:

$$\text{Enrichment}(\%) = \frac{\frac{GFP^{\text{foci}}_{\text{Intensity}}}{GFP^{\text{foci}}_{\text{Area}}} - \frac{\left(GFP^{\text{Nucleus}}_{\text{Intensity}} - GFP^{\text{foci}}_{\text{Intensity}}\right)}{\left(GFP^{\text{Nucleus}}_{\text{Area}} - GFP^{\text{foci}}_{\text{area}}\right)}}{max\left(GFP_{\text{Intensity}}\right)} \times 100$$

Protein expression and purification

Full-length human RBBP4 (residues 1–425) was cloned into the baculovirus expression vector pFBOH-LIC (GenBank EF456740) encoding an N-terminal His_6 tag and a tobacco etch virus protease cleavage site. The protein was expressed in Sf9 cells infected with baculovirus using the Bac-to-Bac expression methodology (Invitrogen). The harvested cells were lysed by rotation in lysis buffer containing 50 mM 4-(2-hydroxyethyl)-1-piperazineethanesulfonic acid (HEPES) pH 7.5, 300 mM NaCl, 5% glycerol, 0.3% NP-40, protease inhibitor cocktail (Roche) and 1000 U of benzonase, followed by centrifugation. The clarified lysate was loaded onto cobalt resin equilibrated with lysis buffer and incubated for 1.5 h with agitation at 4°C. The beads were washed with 50 column volumes of 50 mM Hepes pH 7.5, 300 mM NaCl, 5% glycerol, 10 mM Imidazole. The bound protein was eluted using 50 mM Hepes pH 7.5, 300 mM NaCl, 5% glycerol, 300 mM Imidazole. To cleave the His-tag, eluted protein was dialyzed into dialysis buffer (50 mM Hepes pH 7.5, 300 mM NaCl, 5% glycerol, 2 mM CaCl) with 500 U of Thrombin overnight at 4°C with agitation. The cleaved protein was purified by ion exchange chromatography using a Source S column with an AKTA Explorer (GE Healthcare) and a linear, buffered salt gradient between Buffer A: 20 mM Hepes, 2.5% glycerol and buffer B: 20 mM Hepes, 2.5% glycerol, 1 M NaCl. Fully homogeneous protein was dialyzed back into dialysis buffer.

Structural determination

Cleaved RBBP4 protein was concentrated to 10.0 mg/ml and combined in a 1:1.2 molar ratio with synthetic human PRDM3 or PRDM16 peptide (1–12; Genscript) at 4°C. The complex was crystallized from sitting drops by vapor diffusion from a 1:1 mixture of protein solution and crystallization buffer (20% [PRDM3] or 22% [PRDM16] PEG3350, 0.2 M sodium malonate pH 7, 0.1 M BisTris pH 6). Protein crystals were cryoprotected in well solution containing 33% glycerol in mother liquor. Detraction data for RBBP4:PRDM3 were collected at 100 K using a Rigaku FR-E Superbright rotating anode home source with a Rigaku SATURN A200 detector at a wavelength of 1.54178 Å, while data for RBBP4:PRDM16 were collected at 100 K from a synchrotron source at the Advanced Photon Source from beamline 24-ID-E with an ADSC QUANTUM 315 detector at a wavelength of 0.92819 Å. All data were processed and scaled with XDS (51) and Aimless (52). Initial phases were estimated by molecular replacement using PhaserMR (53) from a known structure of RBBP4 (PDB 4r7a). The structural models were refined using REFMAC5 (54) and manually checked with COOT (55). Each asymmetric unit of the crystals contained two binary peptide:RBBP4 complexes with global identical quaternary architecture. The highly similar PRDM3:RBBP4 and PRDM16:RBBP4 asymmetric units superimposed with a root mean square deviation (r.m.s.d.) of 0.13 Å over 696 Cα atoms, while the PRDM3:RBBP4 and PRDM16:RBBP4 biological assemblies superimposed to the paired, non-crystallographic symmetry mate with r.m.s.d. values of 0.16 and 0.18 Å, respectively. The full β-propeller structure of RBBP4 encompassing all seven WD40 repeats and the N-terminal α-helix were modeled into the electron density, but like other deposited structures, residues 1–3, 89–112, 356–359 and 411–425 could not be modeled due to inadequate electron density at these predicted disordered positions. Electrostatic surface potentials were calculated using the Adaptive Poisson-Boltzmann Solver (APBS) plug-in in PyMOL (56). Images were generated using PyMOL (The PyMOL Molecular Graphics System, v1.7.4, Schrödinger, LLC.).

Isothermal titration calorimetry (ITC)

For isothermal titration calorimetry (ITC) measurements of full-length human RBBP4 (residues 1–425) interactions with PRDM3 and PRDM16 peptides (1–12) and histone H3 peptides (1–25), RBBP4 was dialyzed into a buffer containing 20 mM Hepes, 150 mM NaCl and 2.5% glycerol. Peptides were suspended in the same buffer to a final concentration of 0.50 mM. A preliminary peptide injection of 0.06 μl was followed by subsequent 2-μl injections into the sample cell containing 167 μl of 50 μm RBBP4. The reported K_D and n values are based on the average from three experiments and are accompanied by the standard deviation of the measurements. The data were acquired on a Nano ITC from TA Instruments at 25°C and fitted with an independent-binding site model using NanoAnalyze software (v3.7.0).

In silico alanine scan

Calculation of the changes in theoretical binding free energy upon alanine mutation of each residue of the PRDM3 peptide bound to RBBP4 (pdb: 6bw3) was carried out using ICM-Pro (Molsoft) (57). Briefly, the protein complex was processed to repair missing sidechains and add hydrogens followed by energy minimization to relieve possible atomic clashes. ΔGibbs free energy of binding was calculated for the wild-type PRDM3 peptide and all 10 alanine scan mutants. ΔΔGibbs free energy of binding was determined by ΔG(Mut)-ΔG(WT).

RESULTS

PRDM3 is encoded by the MECOM gene and is depleted in solid tumors

Altered *MECOM* gene expression is commonly associated with initiation and aggressiveness in a variety of hematologic cancers (15). To assess if *MECOM* expression perturbations are common in other cancer types, we examined *MECOM* gene expression using RNA-seq data obtained from TCGA from a variety of solid tumor types. *MECOM* gene expression was defined as the total transcripts detected from any part of the *MECOM* locus. First, total *MECOM* gene expression was compared between autologous healthy and tumor tissue samples from a variety of cancer studies that possessed >10 matched sample pairs (Figure 1A and Supplementary Table S2). Pairwise comparisons between autologous samples revealed statistically significant decreases in *MECOM* expression in renal (KIRC and KIRP), lung (LUSC and LUAD), prostate (PRAD) and breast (BRCA) carcinomas, as well as increased *MECOM* expression in liver (LIHC) and thyroid (THCA) carcinomas, as compared to matched healthy tissue (Figure 1A and Supplementary Table S3).

To examine the underlying features of altered *MECOM* gene expression, we compared the expression of each individual transcripts arising from the *MECOM* locus, across healthy tissue and tumor tissue samples. A total of 10 protein-encoding *MECOM* transcripts are annotated in the TCGA data (Figure 1B). The full-length PRDM3-coding transcript (uc011bpj.1) encodes a protein that possesses an N-terminal PR-SET domain followed by two Zinc finger (ZnF) arrays. Two shorter PRDM3-coding transcripts (uc010hwn.2 and uc003ffl.2) encode intact PR-SET domains, but harbor deletions in the C-terminal half of the protein. The six EVI1-coding transcripts lack the PR-SET domain (ΔPR) but retain some or all of the ZnF arrays. One transcript derived from the MDS1 loci (uc011bpl.1) encodes a short protein truncated in the middle of the PR-SET domain and an additional non-coding transcript (uc003ffo.1) brings the total number of *MECOM*-gene derived transcripts to 11. PCA was used to examine the expression of the 11 *MECOM* transcripts, contrasting healthy and tumor tissues from the TCGA studies that had a significant decrease in *MECOM* gene expression. The set of all 11 *MECOM* transcript expression levels for each patient's tumor and normal tissue were used to compute principal component (PC) values. The PC1 and PC2 values were plotted to explore any potential clustering of the tumor and healthy tissue samples. Interestingly, PC2 distinguished between the majority of healthy and tumor tissue samples, wherein the majority of healthy tissue samples were primarily located along the negative PC2 axis, while most tumor samples localized on the positive axis (Figure 1C). To assess which *MECOM* transcripts accounted for the distinction between healthy and tumor samples within PC2, we examined the PC loading plot, which indicated that the expression of full-length PRDM3 (uc011bpj.1) was the largest contributor for samples appearing along the negative PC2 axis (Figure 1D). Taken together, these findings suggest that expression of the full-length PRDM3 transcript is a major contributor to distinguish healthy from tumor tissue in renal, lung, prostate and breast carcinomas.

N-termini of Prdm3 and Prdm16 interact with the NuRD complex

Despite evidence for the tumor suppressive properties of full-length PRDM3 compared to the N-terminal truncated oncogenic EVI1, the function of the N-terminus remains unclear. Full-length PRDM3 and its closely related paralog PRDM16 possess an ~80 residue unstructured region preceding the PR-SET domain, which are both absent in the N-terminally truncated isoforms (referred to as ΔPR). Although the PR-SET domains of PRDM3 and PRDM16 have been associated with weak, exonuclear KMT activity in the cytoplasm (26), a role in mediating protein–protein interactions has not been described. To investigate the potential role of this region, we performed IP-MS assays using full-length mouse Prdm3 and Prdm16 proteins and their respective ΔPR isoforms (Figure 2A). C-terminally tagged GFP-fusion constructs of the full-length and ΔPR isoforms were individually expressed in T47D ductal carcinoma cells and high-affinity prey proteins were purified after with a stringent, high-salt immunoprecipitation protocol and then identified by mass spectrometry.

Gene ontologies were obtained from the lists of high confidence protein–protein interactions using the DAVID software (version 6.8), to identify enriched ontologies related to 'cellular components', and terms passing a Benjamini FDR cut-off of < 0.001 were compared. As expected, all the bait–prey interactions were enriched for terms associated with

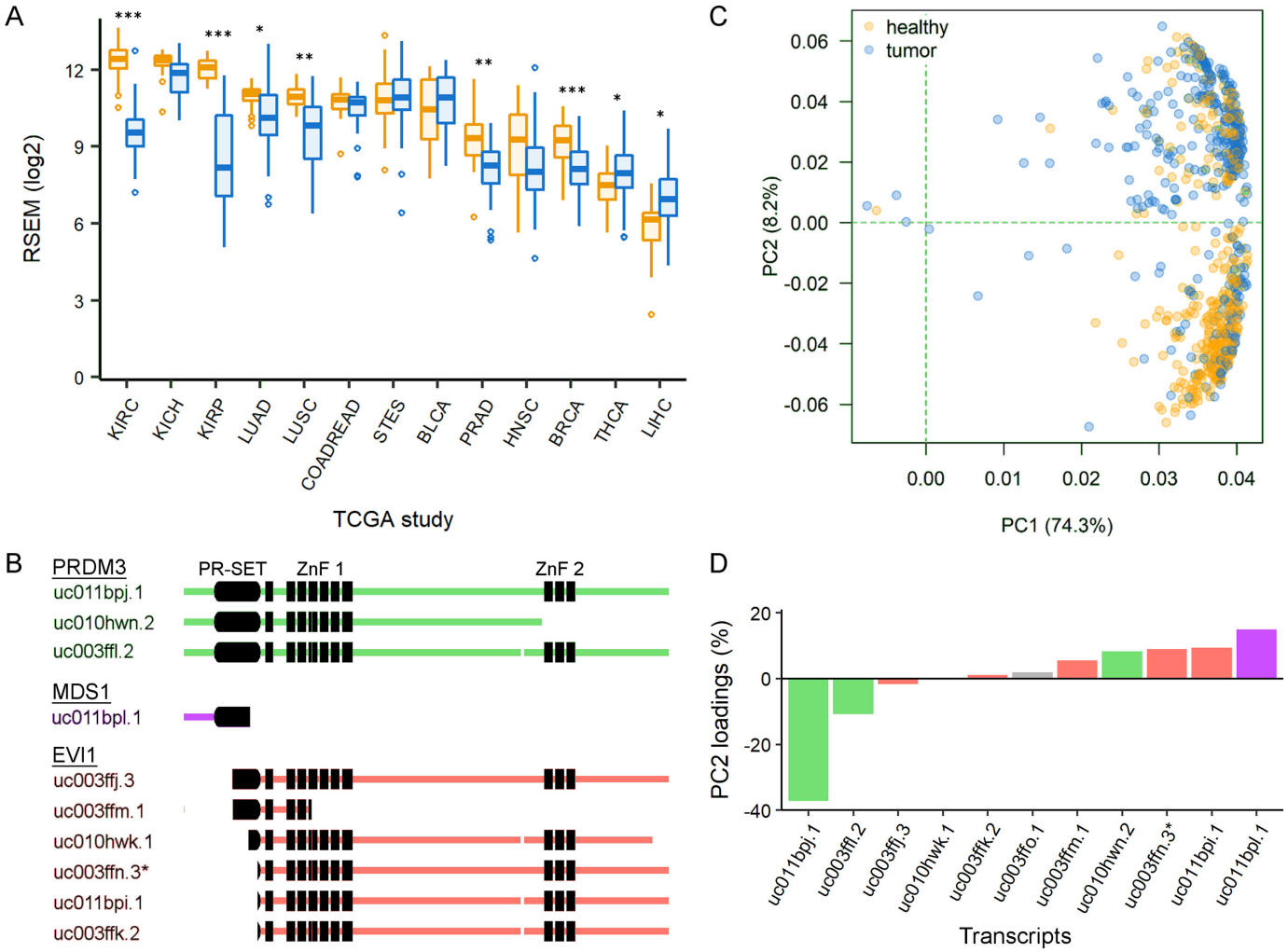

Figure 1. Full-length PRDM3 depletion is prevalent in *MECOM*-deficient solid tumors. (**A**) *MECOM* gene expression analysis in TCGA studies for patient-matched healthy (yellow) and tumor (blue) tissue samples. See Supplementary Tables S1 and S2 for details. (*** q-value $<10^{-9}$, ** q-value $<10^{-4}$, * q-value $<10^{-3}$, Wilcoxon rank-sum test, Bonferroni correction) (**B**) Protein domain diagram of *MECOM* transcripts, which contain the PR-SET domain (referred to as PRDM3 in green) or lack it (referred to as MDS1 in purple and EVI1 in *orange*). Note: uc003ffn.3, uc011bpk.1 and uc003ffi.3 encode an identical amino acid sequence and were grouped as uc003ffn.3*. (**C**) Principle component analysis of *MECOM* isoform expression levels from RNA-seq data comparing patient-matched healthy and tumor tissue samples. (**D**) Principle Component 2 (PC2) loading values of each *MECOM* isoform. Color coding of the ten protein-encoding transcripts correspond to (B), while uc003ffo.1 is a non-coding transcript, shown in gray.

nuclear localization, while both the ΔPR isoforms of Prdm3 and Prdm16 were also associated with exonuclear ontology terms such as 'cytosol' and 'extracellular exosome' (Supplementary Figure S1). Interestingly, only the full-length isoforms were enriched for 'NuRD complex', in agreement with our IP-MS data (Supplementary Figure S1). Indeed, we examined the highest ranked bait–prey interactions of the full-length and ΔPR isoforms or Prdm3 and Prdm16 and found that the NuRD complex members were the most confident interactions with the full-length isoforms, while only RBBP4 and CHD4 were pulled down by the ΔPR isoforms (Figure 2B and C).

To compare NuRD complex member associations between the full-length and ΔPR isoforms, we plotted the spectral count fold-change over that of the GFP-control immunoprecipitation for Prdm3 and Prdm16 (Figure 3A and B). A 4-fold peptide enrichment was observed for full-length over ΔPR isoforms, for significantly called NuRD complex members common to both full-length and ΔPR isoforms (e.g. RBBP4), while most NuRD complex members detected for the full-length isoforms fell bellow the significance threshold or were undetected for the ΔPR bait proteins (Figure 3A and B). We performed co-immunoprecipitation with western blot analysis to directly contrast the interaction between full-length and ΔPR Prdm3 and Prdm16 isoforms with members of the core NuRD complex. Western blot analysis confirmed that the full-length Prdm3 and Prdm16 isoforms associated with RBBP4, MTA1 and HDAC2, while associations with the ΔPR isoforms were not detected (Figure 3C). To further validate this interaction for the endogenous human proteins, we preformed reciprocal co-immunoprecipitations in high EVI1 expressing T47D cells and high PRDM3 expressing MCF7 cells. Western blot analysis after the co-immunoprecipitation of endogenous RBBP4 demonstrated that endogenous, human PRDM3 protein associated with

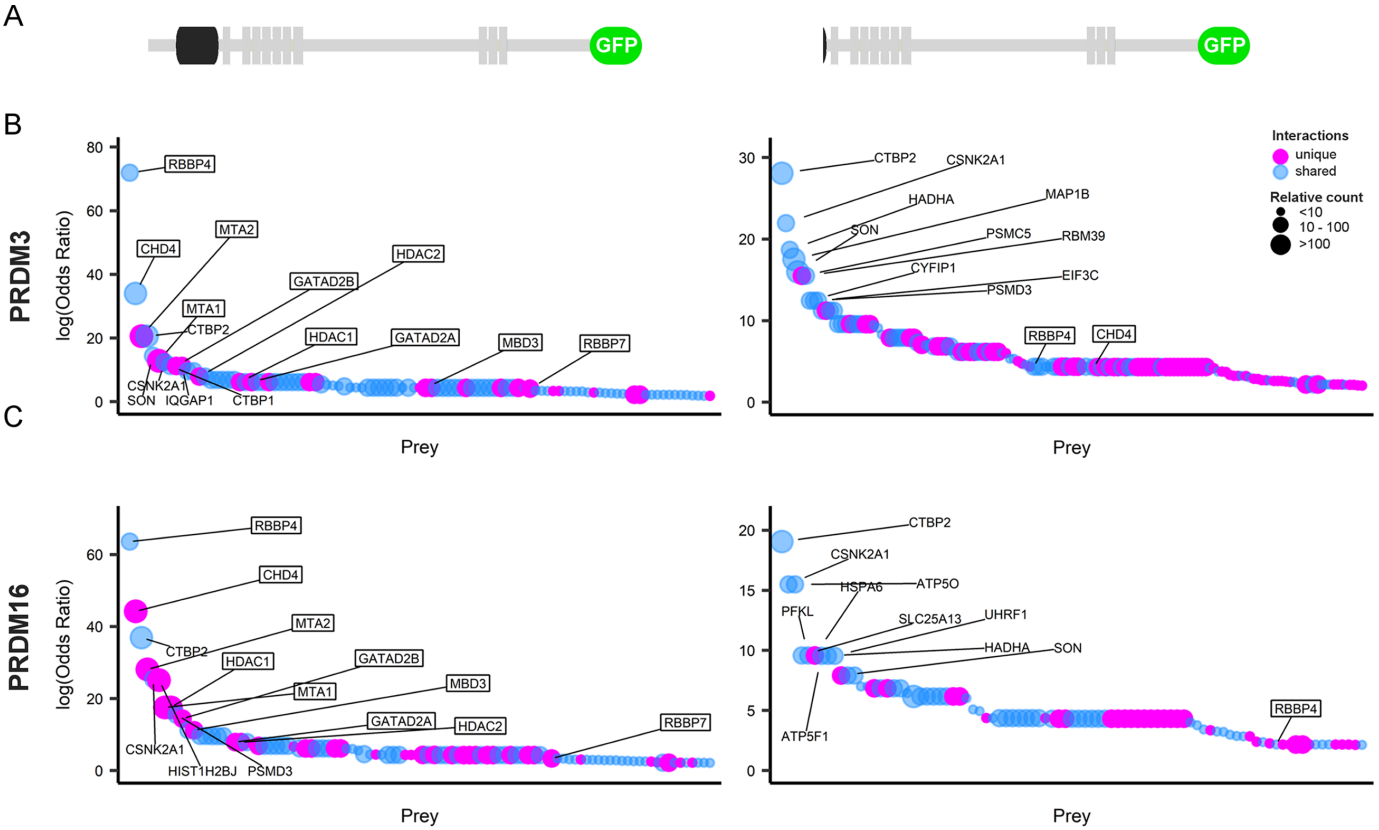

Figure 2. The N-termini of full-length PRDM3 and PRDM16 isoforms function as protein–protein interaction scaffolds. (**A**) Protein domain diagram of full-length (left) and ΔPR (right) PRDM3 and PRDM16 isoforms used for co-immunoprecipitation with mass spectrometry. (**B** and **C**) Prey proteins associated with PRDM3 (B) and PRDM16 (C) by co-immunoprecipitation with the full-length (left) and ΔPR (right) bait. Prey proteins scoring with a BFDR ≤ 1% are ranked by decreasing Odds ratio relative to GFP control co-immunoprecipitation. Prey proteins shared between full-length and ΔPR isoforms are indicated by color and peptide count relative to GFP control is indicated by size. NuRD complex members are outlined.

RBBP4, while EVI1 was not detected (Supplementary Figure S2). These findings indicate that the N-terminal region of full-length PRDM3 and PRDM16 are key mediators of the NuRD complex interaction.

N-termini of PRDM3 and PRDM16 bind directly to RBBP4

We hypothesized that the residues that facilitated the interaction with NuRD would be conserved between PRDM3 and PRDM16. As expected the PR-SET domains are highly conserved among both the mouse and human proteins, as are two short sequence regions N-terminal to the PR-SET domains (Supplementary Figure S3A). Interestingly, the first 12 residues of both proteins also share close sequence identity with the N-terminal residues of histone H3 (Supplementary Figure S4A), which has been shown to interact with the RBBP4 *Drosophila* paralog Nurf55 (40). To assess the potential role of the 12 aa peptide regions versus the PR domains for NuRD complex interactions, we purified proteins comprised of the first ∼200 residues of human PRDM3 and PRDM16 with and without these 12 residues and performed *in vitro* pull-down assays with purified recombinant RBBP4, which had the highest likelihood of interaction calculated by SAINTexpress for both full-length PRDM3 and PRDM16 among all the bait–prey interactions in our IP-MS datasets (Figure 3B and C). Recombinant RBBP4 only associated with the first ∼200 N-terminal residues of PRDM3 and PRDM16 *in vitro* when the first 12 amino acids were also present (Supplementary Figure S3B).

We next preformed peptide-binding assays by ITC to assess the interaction between residues 1–12 of human PRDM3 and PRDM16 with full-length RBBP4. Equilibrium dissociation constants (K_D) with a 1:1 binding ratio between peptide and RBBP4 were calculated to be 2.96 ± 0.34 μM and 3.15 ± 0.36 μM for PRDM3 and PRDM16 peptides, respectively (Figure 4A and B). By comparison, a histone H3 peptide (residues 1–25) bound to human RBBP4 with a K_D of 1.50 ± 0.38 μM (Figure 4C). Examination of the crystal structure of a histone H3 peptide with Nurf55, suggested that lysine 4 of H3 (H3K4) is important for RBBP4 interactions (Supplementary Figure S4B). As a control for peptide binding to RBBP4, we tested the affinity of a 25-residue histone H3 peptide bearing a trimethylated lysine 4 (H3K4me3) and observed that the K_D decreased by 10-fold relative to the unmodified peptide (Supplementary Figure S4C). This suggested that the lysine conserved among histone H3, PRDM3 and PRDM16 may be an important contributor to the interaction.

To investigate the importance of the 12 N-terminal residues of the full-length isoforms in a cellular context, we assessed co-localization of PRDM3 with RBBP4 by employing a LacO/LacR chromatin immobilization assay.

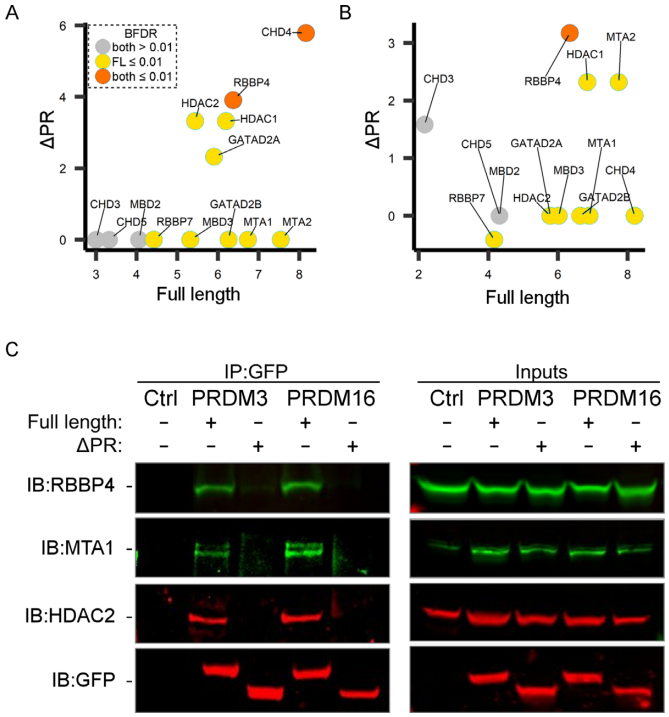

Figure 3. The NuRD complex members are enriched interactors with full-length PRDM3 and PRDM16. (**A** and **B**) Spectral count fold change above control (log2) of the NuRD complex members that co-immunoprecipitated with (A) PRDM3 and (B) PRDM16 comparing full-length (*x*-axis) and ΔPR (*y*-axis) bait. (**C**) Immunoblotting of specific NuRD complex members following co-immunoprecipitation with full-length and ΔPR isoforms of PRDM3 and PRDM16. Ten percent protein input is shown in the right-hand panel. GFP empty vector was used as a control (Ctrl). Blots shown are representative of three experiments.

Table 1. Data for X-ray Crystal Structure of PRDM3/16 (1–12aa) with RBBP4.

PDB structure	6bw3	6bw4
Contents	RBBP4 and PRDM3(1–12aa)	RBBP4 and PRDM16(1–12aa)
Data collection		
Space group	P 1 2_1 1	P 1 2_1 1
wavelength (Å)	1.54178	0.97918
a, *b*, *c* (Å)	75.98,59.82,101.77	76.03,59.86,101.84
α, β, γ (°)	90, 94.55, 90	90, 94.55, 90
Resolution (Å)	46.95-2.2 (2.27-2.2)	19.78-2.0 (2.05-2.0)
R_{merge} (%)	0.1 (0.1)	0.06 (0.7)
$I/\sigma(I)$	2.44	2.75
Completeness (%)	99.4	99.2
Redundancy	4.1 (4.0)	3.9 (4.1)
Refinement		
Resolution (Å)	46.95 - 2.2	19.78 - 2.0
Reflections	44 059	58 442
R_{work}/R_{free}	0.215/0.246	0.199/0.233
Wilson B factor (Å^2)	34.0	34.8
Protein atoms	5841	5877
Water molecules	110	112
Unidentified molecules	12	12
r.m.s.d. values		
Bond length (Å)	0.011	0.012
Bond angle (°)	1.48	0.95
Ramachandran values		
Favored (%)	96.1	97.2
Allowed (%)	3.5	2.5
Outliers (%)	0.4	0.3

*Values in parentheses are for high-resolution shell.
R-Factor = $\Sigma\, hkl\, \|\|F_o|-|F_c\|\| / \Sigma\, hkl\, |F_o|$, where F_o and F_c are the observed and calculated structure factor amplitudes for reflection *hkl*.
R_{free} is calculated against a 5% random sampling of the reflections that were removed before structure refinement.
r.m.s.d. = root mean squared deviation.

U2OS cells with a stably integrated 256 LacO array were transfected with C-terminally tagged PRDM3-mCherry-LacR-NLS with either wild-type (WT) PRDM3 or PRDM3 lacking the 12 N-terminal residues (PRDM3$^{\Delta N12}$) to assess for co-localization with co-expressed GFP-RBBP4. PRDM3-LacR fusion proteins localized at the LacO array as single red foci (Figure 4D and Supplementary Figure S5). GFP-RBBP4 colocalized in clear foci with WT PRDM3-LacR, but not with PRDM3$^{\Delta N12}$ or the control (Figure 4D). When co-expressed with PRDM3$^{\Delta N12}$, GFP-RBBP4 produced a diffuse GFP signal in both the nucleus and the cytoplasm. In some cells, weak GFP foci could be spotted slightly above background GFP fluorescence in the PRDM3$^{\Delta N12}$-expressing cells, as well as in N-terminally tagged PRDM3$^{\Delta N12}$-expressing cells (Supplementary Figure S5). Quantification of the GFP signal increase at the mCherry foci normalized to the background nuclear GFP fluorescence showed a significant increase in signal intensity with WT and mutant PRDM3 proteins ($P < 10^{-16}$, ANOVA/Dunnett analysis; Figure 4E). Taken together with the immunoprecipitation and affinity pull-down assays, these results show that the 12 N-terminal residues of full-length PRDM3 and PRDM16 are essential for the interaction with RBBP4 in a cellular environment.

Co-crystal structure of RBBP4 with PRDM3/PRDM16 N-terminal peptide

RBBP4 helps direct the NuRD complex onto chromatin via associations with the histone H3 tail, but transcription factors can also serve as an intermediary between the NuRD complex and chromatin by competing for occupancy at the histone H3 interface on RBBP4 (40,42–44). To examine the structural basis of the interaction between PRDM3 and PRDM16 with RBBP4, we determined the crystal structures of full-length RBBP4 (residues 1–425) bound to human PRDM3 and PRDM16 peptides (residues 1–12) at 2.2 and 2.0 Å, respectively (Figure 5A and B; Table 1). The nearly identical structures of the PRDM3 and PRDM16 peptides bound to RBBP4 revealed that both peptides bind to the electronegative histone H3-binding interface of RBBP4 in an extended conformation (Figure 5 and Supplementary Figure S6).

The peptide:RBBP4 interactions are similar to histone H3 on Nurf55 (40) and include salt bridges, hydrogen bonds, hydrophobic contacts and cation–π stacking (Figure 6A and Supplementary Table S4). At the N-terminus, the positively charged amine groups of the Met1 residues of PRDM3 and PRDM16 form salt bridges with Asp248 and Glu231 on RBBP4 (Figure 6B). Prominently, the positively charged Arg2 and Lys4 sidechains orient toward the highly electronegative RBBP4 β-propeller axis where the

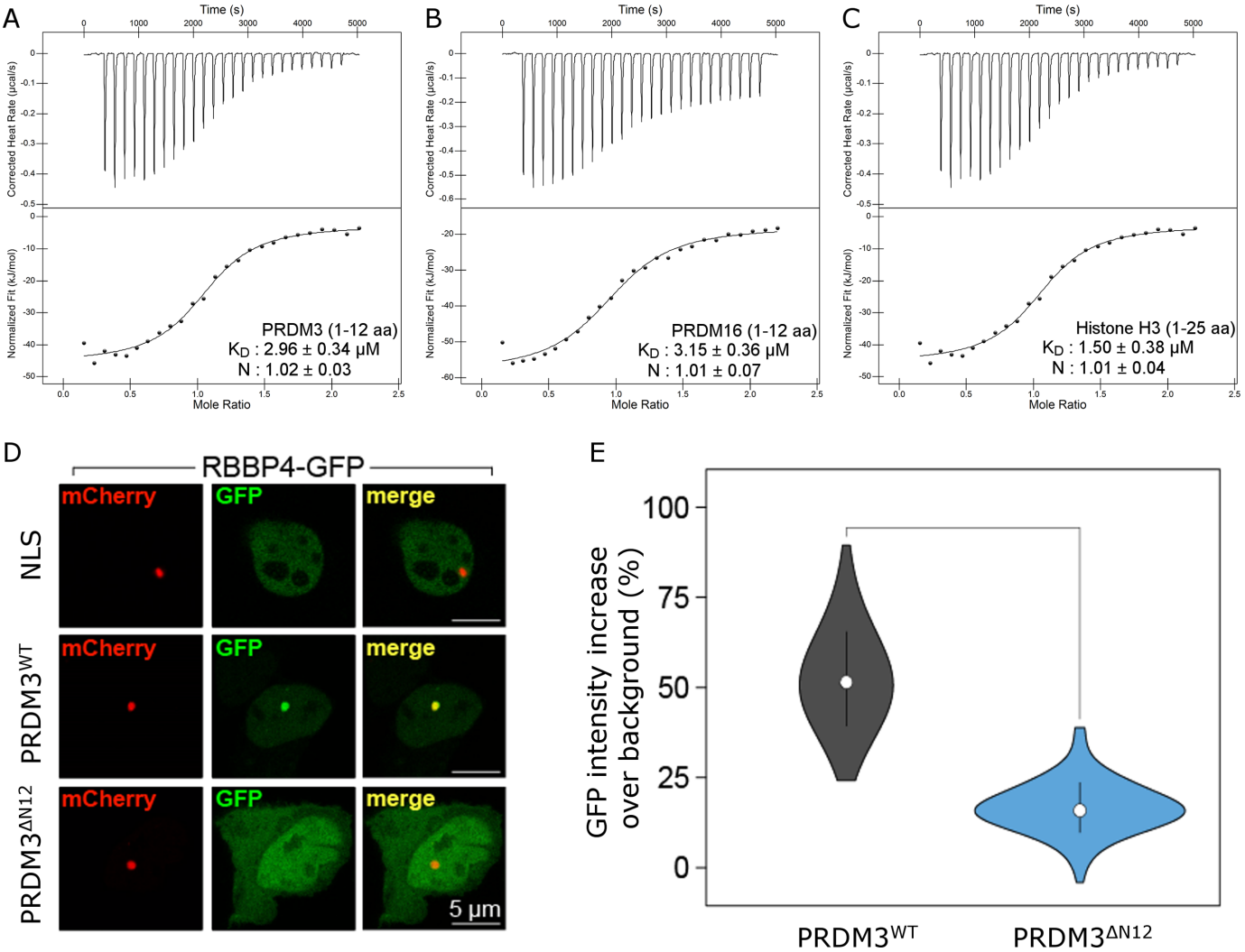

Figure 4. The first 12 residues of PRDM3/16 interact with RBBP4. (**A–C**) *In vitro* measurement of dissociation constant (K_D) and molar stoichiometry (N) of (A) PRDM3, (B) PRDM16 and (C) Histone H3 peptides with RBBP4 measured by ITC (experiment performed in triplicate, standard deviation is shown). (**D**) Cellular interaction between PRDM3 and RBBP4 measured by LacO/LacR chromatin immobilization assay. PRDM3-mCherry-LacR-NLS with WT PRDM3 or PRDM3 lacking the 12 N-terminal residues (ΔN12) were assessed for co-localization with GFP-RBBP4. (**E**) Quantification of the PRDM3 (WT or ΔN12) co-localization with RBBP4 shown in (D). The violin plots represent the GFP intensity increase over background in the mCherry foci, calculated from $n = 100$ cells.

Arg2 guanidinium moiety is sandwiched between the aromatic sidechains of Tyr181 and Phe321 forming stabilizing cation–π interactions, while additionally participating in a salt bridge and hydrogen bond network with Glu231, Arg129, Glu231 and Asn277 (Figure 6B). The cationic ε-amino group of Lys4 forms salt bridges with Glu179 and Glu126, and hydrogen bonds with Tyr181 and Asn128, with hydrophobic packing of the aliphatic component of the sidechain against the sidechain of Leu45 (Figure 6C). As reported from Thr2 of histone H3 on Nurf55 (40), Ser3 from PRDM3 and PRDM16 is solvent exposed and does not interact with RBBP4 directly. Weak electron density for the Arg6 and Arg8 sidechains was only apparent in some biological assemblies of PRDM3:RBBP4 and PRDM16:RBBP4, suggesting that the salt bridges of Arg6 with Asp74 and Arg8 with Glu75 and Glu42 may not be important contributors to the peptide:RBBP4 interaction (Figure 6D). The aliphatic and cationic regions of the Lys9 sidechain form hydrophobic and polar contacts with the aliphatic and anionic regions of the Glu41 sidechain, respectively, as well as a salt bridge with Glu75 (Figure 6E). The electron density of Leu10 was inadequate to distinguish the position of its sidechain or the subsequent resides (Supplementary Figure S7), while the important interactions with RBBP4 occur with residues 1–9 of both peptides. To assess the validity of our structural model, we preformed an *in silico* alanine scan of the PRDM3 peptide and calculated the difference in Gibbs binding energy between the wild-type and mutant peptides (Supplementary Figure S8A). The Lys4 sidechain had the largest theoretical contribution to RBBP4 binding and a K4A mutant peptide of PRDM3 (1–12) lacked detectable binding to RBBP4 as measured by ITC (Supplementary Figure S8B).

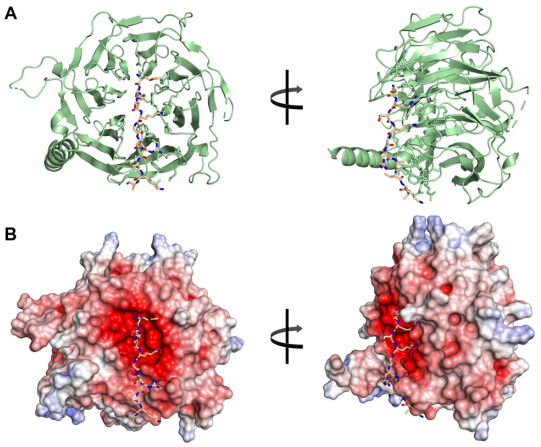

Figure 5. Crystal structure of RBBP4 in complex with the PRDM3 (1–12 amino acid) peptide. (**A**) Stick representation of PRDM3 (1–12) peptide [Oxygen atoms (red) and nitrogen (blue)] bound to the ribbon representation of RBBP4. (**B**) Electrostatic surface potential representation of the binding pocket with aligned PRDM3 peptide. RBBP4 surface color indicates electrostatic potential ranging from −7kT/e (red) to +7kT/e (blue). Electrostatic surface potentials were calculated using the APBS.

Our structural elucidation of the PRDM3 and PRDM16 peptides bound to RBBP4 revealed a conserved interaction network common to other RBBP4 interacting proteins that binding perpendicular to the β-propeller axis. The N-terminal PRDM3 and PRDM16 peptides share higher sequence identity with the histone H3 peptide than all other peptides from transcription factors known to bind RBBP4 (Figure 7C). Sequence and structural alignments of RBBP4-binding peptides at the β-propeller axis clearly demonstrate the importance of the conserved arginine-lysine pair, which makes critical contacts at the highly electronegative groove on RBBP4 (Figure 7A–C). Notably, the small and polar Thr3 residue found between the arginine and lysine residues of histone H3 is replaced with a Ser in PRDM3 and PRDM16, while this residue is absent in all other previously identified binding peptides, (Figure 7B and C). These small and polar residues do not form direct interactions with RBBP4, but instead extend the peptide backbone to enable consistent sidechain orientation towards RBBP4 (Figure 7B). Additionally, an alanine residue is found at position 7 of histone H3 and PRDM3/16, which is a proline in all other structures, further exemplifying the peptide backbone similarity with histone H3 that is exclusive to PRDM3 and PRDM16 (Figure 7C).

DISCUSSION

The Yin-Yang paradigm of oncogenesis describes a situation where an imbalance between an oncogene and a tumor suppressor encoded by the same gene gives rise to cancer (11). The differential expression of short, oncogenic and long, tumor suppressive isoforms has been reported for several PRDM family members, including PRDM1, PRDM2, PRDM3, PRDM5 and PRDM16 (23,58–61). It is well established that chromosomal aberrations at the PRDM3-encoding gene, *MECOM*, are found in up to 10% of AML cases with poor survival outcomes (13,14). The expression levels of specific *MECOM* isoforms suggests that the N-terminal residues of PRDM3 bestow a tumor suppressor function, while the oncogenic shorter EVI1 isoform is overexpressed in myeloid, ovarian, liver and colon tumors, and correlates with poor outcome in AML (1,12,13,15–18). Indeed, this is supported by our comparative analysis of *MECOM* isoform expression between patient-matched tumor and healthy tissues and identified a previously unreported loss of full-length PRDM3 expression as a common feature of certain solid tumor types, such as renal, lung, prostate and breast carcinomas.

To further our understanding towards a potential disease mechanism, we searched for unique molecular characteristics of the full-length PRDM3 protein that may explain the Yin-Yang paradigm. We used IP-MS experiments to directly compare the potential protein–protein interactions between the full-length and ΔPR isoforms of the PRDM3 and PRDM16 paralogs and present the molecular basis for a novel protein–protein interaction that is unique to the full-length isoforms. Specifically, the first 10 N-terminal residues of full-length PRDM3 and PRDM16 directly engage the NuRD chromatin remodeling complex via the histone H3 binding interface on RBBP4. We propose a model in which this interaction recruits the NuRD complex to genomic loci specifically bound by the full-length protein isoforms of PRDM3 and PRDM16 (Figure 7D).

The full-length PRDM3 and PRDM16 proteins possess an N-terminal ∼80 residue unstructured region followed by the PR-SET domain, which are both absent in the ΔPR isoforms. While the PR-SET domains have been reported to have weak intrinsic KMT activity, reports have been inconsistent in identifying either H3K4 or H3K9 as the substrate in either the nucleus or cytosol (25–27). PRDM3 is also known to interact with established KMT enzymes such as G9a and SUV39H1 (62), which could potentially contribute trace KMT activity to preparations or PRDM3 that contain trace amounts of these robust enzymes. Moreover, both PRDM3 and PRDM16 lack a key catalytic tyrosine residue conserved in all other established SET-domain KMT enzymes (Supplementary Figure S9). Therefore, we hypothesized that there may be an alternative activity attributed to the N-terminal region missing from oncogenic ΔPR isoforms. We focused on potential protein–protein interactions, which could account for molecular functions across the PR-SET domain as well as the preceding unstructured residues in the full-length proteins. Unlike previous studies, our IP-MS experiments are the first to directly compare the potential protein–protein interactions found for the full-length and ΔPR isoforms of the PRDM3 and PRDM16 paralogs. We show that the previously demonstrated interactions between EVI1 and epigenetic factors like the CtBP proteins and the CSNK2A1 and CSNK2B components of the CK2 complex (34,46) were also found for the full-length PRDM3 protein, as well as both the full-length and ΔPR PRDM16 protein isoforms. Using a yeast two-hybrid screen, Spensberger *et al*. found that EVI1 interacts specifically with the NuRD complex member MBD3b (47). However, in a subsequent study performed by Bard-Chapeau *et al*., who used proteomic IP-MS experiments in an ovarian cancer cell line, showed that while RBBP4, HDAC1, HDAC2 and CHD4 were associated with EVl1,

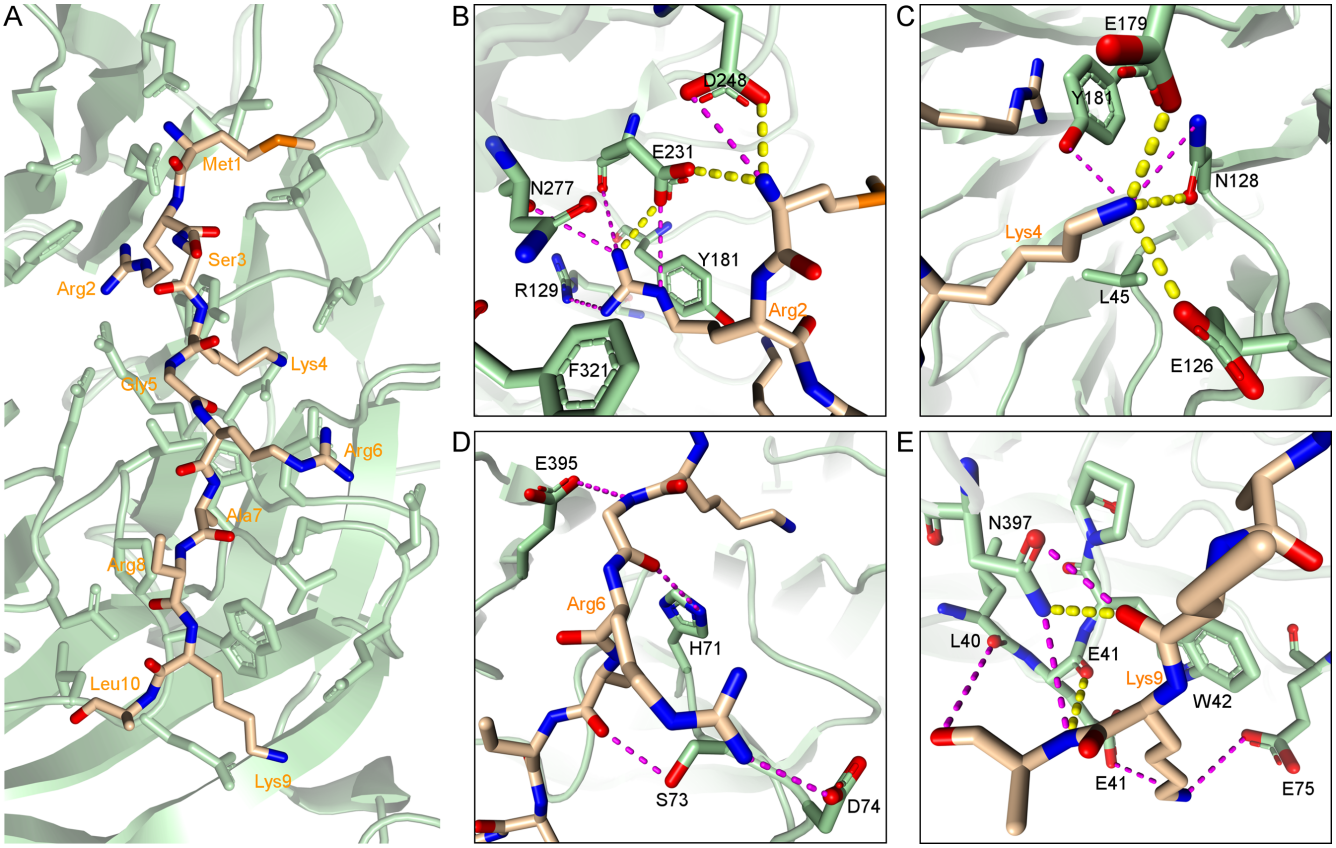

Figure 6. Amino acid interactions at the PRDM3 peptide-RBBP4 interface. (**A**) The interface between PRDM3 (1–12) residues (tan) and RBBP4 residues (green). Interactions between PRDM3 centered at (**B**) arginine 2, (**C**) lysine 4, (**D**) arginine 6 and (**E**) lysine 9 are indicated with dashed lines. Interactions within 4 Å (purple) and 3 Å (yellow) are detailed in Supplementary Table S4.

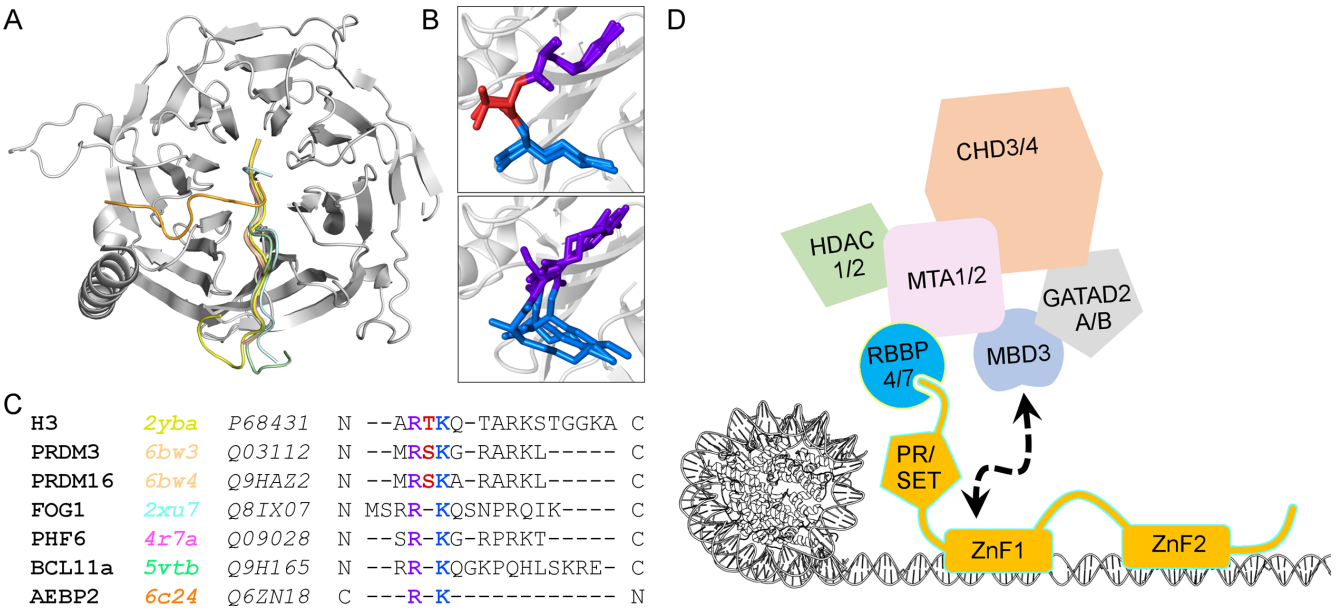

Figure 7. PRDM3 and PRDM16 mimic the RBBP4-histone H3 interaction. (**A**) Structure alignment of all reported peptides that bind perpendicular to the RBBP4 β-propeller axis. (**B**) Structure alignment of arginine, threonine/serine and lysine from H3, PRDM3 and PRDM16 (top) and arginine and lysine from FOG1, PHF6, BCL11a and AEBP2 (bottom). (**C**) Sequence alignment of all reported peptides that bind to the RBBP4 top hole. Colors correspond to A and B panels. (**D**) A model illustrating a potential mechanism for how full-length PRDM3 and PRDM16 could tethering the NuRD complex to chromatin and subsequently regulate transcription. Dashed line and arrows indicate potential secondary interactions between MBD3 of NuRD and the first zinc finger motifs of PRDM3 and PRDM16.

MBD3b was not detected (46). Through our proteomics IP-MS experiments, we found that while both the full-length and ΔPR isoforms of the PRDM3 and PRDM16 proteins associated with some NuRD complex members like RBBP4 and CHD4, only the full-length isoforms were able to pull-down the complete NuRD complex. Furthermore, our co-IP experiments demonstrated that the associations between the ΔPR isoforms and RBBP4 fall below the assay's detection threshold. Additionally, the EVI1 protein has been demonstrated to form homo-oligomers (36), but it is unclear if EVI1 and PRDM3 can form hetero-oligomers. A hetero-dimerization event could explain how the ΔPR proteins could indirectly associate with the NuRD complex through their longer counterparts, which would justify a weaker relative association with NuRD complex members. Taken together, our proteomics and structural data suggest that the full-length PRDM3 and PRDM16 proteins form a stable complex with NuRD and therefore we hypothesize that the full-length isoforms can direct NuRD to specific genomic loci, while EVI1 and ΔPR PRDM16 likely lack this ability due to a weaker association.

The NuRD chromatin remodeling complex has been implicated in both promotion and suppression of tumorigenesis, growth and metastasis (37,63). This paradoxical behavior emerges from its ability to epigenetically regulate genes for either tumor suppressors or oncogenic factors depending on specific associations with genomic localization factors. Multiple studies have demonstrated that the NuRD complex can associate with oncogenic transcription factors like BCL11A via RBBP4 in triple-negative breast cancer (44), TWIST via MTA2 to drive metastasis in carcinomas (64) and NAB2 via CHD4 in prostate cancers (65). Additionally, NuRD also associates with tumor suppressing transcription factors like PHF6 (43) and SALL1 (41) via RBBP4, as well as c-JUN via MBD3 (66). RBBP4 and RBBP7 are integral components of the core NuRD complex, serving as a scaffold for the MTA proteins, while functioning as chromatin recognition interfaces through binding to the histone H3 tail. A previous ChIP-seq analysis of CHD4 showed that the NuRD complex localized at genomic loci marked by trimethylated lysine 4 on histone H3 (H3K4me3), which is a post-translational modification incompatible with RBBP4/7 binding (40,67). Interestingly, BCL11A, PHF6, SALL1 and FOG1 all interact with NuRD by competing for RBBP4/7 at the histone H3-binding interface, thereby demonstrating how NuRD localization can depend on the balance of transcription factors available within specific nuclear environments.

Given that PRDM3 and PRDM16 directly interact with NuRD via RBBP4, it is noteworthy that we did not identify any other RBBP4/7 containing complexes in our IP-MS experiments. The RBBP4 and RBBP7 paralogs share a 90% sequence identity with effectively identical histone H3 binding interfaces. Other RBBP4-binding transcription factors like PHF6 and FOG1 have also been found to exclusively associate with NuRD (42,43), while alternatively, BCL11A was demonstrated to bind RBBP4 in the NuRD, PRC2, and SIN3A complexes (44). Structural studies have shown that when RBBP4 is found in PRC2, the histone H3 binding interface is engaged by either AEBP2 or SUZ12. While we observed that a histone H3 peptide binds roughly twice as tightly to RBBP4 than PRDM3 and PRDM16 peptides, competitive binding assays between BCL11A and histone H3 peptides suggest that BCL11A has a three times greater affinity for RBBP4, which may explain why it is capable of binding multiple RBBP4-containing complexes (44). Furthermore, the potential of multivalent interactions between PRDM3 and PRDM16 with the NURD complex remains unexplored. Studies have shown that the transcription factor FOG1 binds to the MTA proteins and RBBP4 in NuRD (42,45) and it would be likely that a conserved region between EVI1 and the ΔPR PRDM16 proteins could facilitate this secondary interaction, perhaps on MBD3b. While we did not observe that MBD3 associated with either of the ΔPR proteins, it is interesting that MBD3 deletions have been implicated in cancer progression (68).

In summary, we have identified an important function of the N-termini of PRDM3 and PRDM16, which bind directly to RBBP4 to facilitate an interaction with the NuRD chromatin remodeling complex. Our data is consistent with a model in which full-length PRDM3 and PRDM16 proteins function as transcriptional co-repressors by directing NuRD to specific genomic loci. The truncation of the N-terminus dramatically decreases the interaction, which warrants further investigation into the resulting transcriptional changes and could suggest a mechanism for the tumor-suppressive properties of full-length PRDMs through their interaction with RBBP4/NuRD.

DATA AVAILABILITY

Atomic coordinates and structure factors for the reported crystal structures have been deposited with the Protein Data Bank under accession codes 6bw3 and 6bw4.

SUPPLEMENTARY DATA

Supplementary Data are available at NAR Online.

ACKNOWLEDGEMENTS

We thank Advanced Photon Source for access to beamline 24-ID-E and the members of the Arrowsmith lab, the Structural Genomics Consortium and Robert M Campbell for critical review of the manuscript and constructive discussions. We also thank Thomas Jenuwein for providing the plasmids for mouse Prdm3 and Prdm16 full-length and truncated isoforms.

FUNDING

Natural Sciences and Engineering Research Council [PGSD3 to D.I., RGPIN-2015-05939 to C.H.A]; Canadian Institutes of Health Research [FDN154328 to C.H.A., MOP272138 to J.G.]; Lilly Research Award Program (LRAP) to C.H.A.; Medical Research Council [MR/N010051/1 to P.F.]; Luxembourg National Research Fund (to E.L.-F.); Marie Curie Actions of the European Commission [FP7-COFUND to E.L.-F.]; Canadian Institutes of Health Research Banting Postdoctoral Fellowship (to E.L.-F.); The Structural Genomics Consortium is a registered charity (no: 1097737) that receives funds

from AbbVie; Bayer Pharma AG; Boehringer Ingelheim; Canada Foundation for Innovation; Eshelman Institute for Innovation; Genome Canada through Ontario Genomics Institute [OGI-055]; Innovative Medicines Initiative (EU/EFPIA) [ULTRA-DD: 115766]; Janssen, Merck & Co.; Novartis Pharma AG; Ontario Ministry of Research Innovation and Science (MRIS); Pfizer, São Paulo Research Foundation-FAPESP, Takeda and the Wellcome Trust. Funding for open access charge: Canadian Institutes of Health Research [FDN154328].
Conflict of interest statement. None declared.

REFERENCES

1. Fears,S., Mathieu,C., Zeleznik-Le,N., Huang,S., Rowley,J. and Nucifora,G. (1996) Intergenic splicing of MDS1 and EVI1 occurs in normal tissues as well as in myeloid leukemia and produces a new member of the PR domain family. *Proc. Natl. Acad. Sci. U.S.A.*, **93**, 1642–1647.
2. Yoshida,M., Nosaka,K., Yasunaga,J., Nishikata,I., Morishita,K. and Matsuoka,M. (2004) Aberrant expression of the MEL1S gene identified in association with hypomethylation in adult T-cell leukemia cells. *Blood*, **103**, 2753–2760.
3. Fagerberg,L., Hallström,B., Oksvold,P., Kampf,C., Djureinovic,D., Odeberg,J., Habuka,M., Tahmasebpoor,S., Danielsson,A., Edlund,K. *et al.* (2014) Analysis of the human tissue-specific expression by genome-wide integration of transcriptomics and antibody-based proteomics. *Mol. Cell. Proteomics*, **13**, 397–406.
4. Hohenauer,T. and Moore,A. (2012) The Prdm family: expanding roles in stem cells and development. *Development*, **139**, 2267–2282.
5. Zhang,Y., Stehling-Sun,S., Lezon-Geyda,K., Juneja,S., Coillard,L., Chatterjee,G., Wuertzer,C., Camargo,F. and Perkins,A. (2011) PR-domain-containing Mds1-Evi1 is critical for long-term hematopoietic stem cell function. *Blood*, **118**, 3853–3861.
6. Chuikov,S., Levi,B., Smith,M. and Morrison,S. (2010) Prdm16 promotes stem cell maintenance in multiple tissues, partly by regulating oxidative stress. *Nat. Cell Biol.*, **12**, 999–1006.
7. Aguilo,F., Avagyan,S., Labar,A., Sevilla,A., Lee,D., Kumar,P., Lemischka,I., Zhou,B. and Snoeck,H. (2011) Prdm16 is a physiologic regulator of hematopoietic stem cells. *Blood*, **117**, 5057–5066.
8. Seale,P., Kajimura,S., Yang,W., Chin,S., Rohas,L., Uldry,M., Tavernier,G., Langin,D. and Spiegelman,B. (2007) Transcriptional control of brown fat determination by PRDM16. *Cell. Metab.*, **6**, 38–54.
9. Huang,L., Pan,D., Chen,Q., Zhu,L., Ou,J., Wabitsch,M. and Wang,Y. (2017) Transcription factor Hlx controls a systematic switch from white to brown fat through Prdm16-mediated co-activation. *Nat. Commun.*, **8**, 68.
10. Harms,M., Lim,H., Ho,Y., Shapira,S., Ishibashi,J., Rajakumari,S., Steger,D., Lazar,M., Won,K. and Seale,P. (2015) PRDM16 binds MED1 and controls chromatin architecture to determine a brown fat transcriptional program. *Genes Dev.*, **29**, 298–307.
11. Mzoughi,S., Tan,Y., Low,D. and Guccione,E. (2016) The role of PRDMs in cancer: one family, two sides. *Curr. Opin. Genet. Dev.*, **36**, 83–91.
12. Morishita,K., Parganas,E., William,C., Whittaker,M., Drabkin,H., Oval,J., Taetle,R., Valentine,M. and Ihle,J. (1992) Activation of EVI1 gene expression in human acute myelogenous leukemias by translocations spanning 300–400 kilobases on chromosome band 3q26. *Proc. Natl. Acad. Sci. U.S.A.*, **89**, 3937–3941.
13. Lugthart,S., van Drunen,E., van Norden,Y., van Hoven,A., Erpelinck,C., Valk,P., Beverloo,H., Löwenberg,B. and Delwel,R. (2008) High EVI1 levels predict adverse outcome in acute myeloid leukemia: prevalence of EVI1 overexpression and chromosome 3q26 abnormalities underestimated. *Blood*, **111**, 4329–4337.
14. Gröschel,S., Lugthart,S., Schlenk,R., Valk,P., Eiwen,K., Goudswaard,C., van Putten,W., Kayser,S., Verdonck,L., Lübbert,M. *et al.* (2010) High EVI1 expression predicts outcome in younger adult patients with acute myeloid leukemia and is associated with distinct cytogenetic abnormalities. *J. Clin. Oncol.*, **28**, 2101–2107.
15. Baldazzi,C., Luatti,S., Zuffa,E., Papayannidis,C., Ottaviani,E., Marzocchi,G., Ameli,G., Bardi,M., Bonaldi,L., Paolini,R. *et al.* (2016) Complex chromosomal rearrangements leading to MECOM overexpression are recurrent in myeloid malignancies with various 3q abnormalities. *Genes Chromosomes Cancer*, **55**, 375–388.
16. Brooks,D., Woodward,S., Thompson,F., Dos Santos,B., Russell,M., Yang,J., Guan,X., Trent,J., Alberts,D. and Taetle,R. (1996) Expression of the zinc finger gene EVI-1 in ovarian and other cancers. *Br. J. Cancer*, **74**, 1518–1525.
17. Yasui,K., Konishi,C., Gen,Y., Endo,M., Dohi,O., Tomie,A., Kitaichi,T., Yamada,N., Iwai,N. *et al.* (2015) EVI1, a target gene for amplification at 3q26, antagonizes transforming growth factor-β-mediated growth inhibition in hepatocellular carcinoma. *Cancer Sci.*, **106**, 929–937.
18. Nayak,K., Sajitha,I., Kumar,T. and Chakraborty,S. (2018) Ecotropic viral integration site 1 promotes metastasis independent of epithelial mesenchymal transition in colon cancer cells. *Cell Death Dis.*, **9**, 18.
19. Haas,K., Kundi,M., Sperr,W., Esterbauer,H., Ludwig,W., Ratei,R., Koller,E., Gruener,H., Sauerland,C., Fonatsch,C. *et al.* (2008) Expression and prognostic significance of different mRNA 5′-end variants of the oncogene EVI1 in 266 patients with de novo AML: EVI1 and MDS1/EVI1 overexpression both predict short remission duration. *Genes Chromosomes Cancer*, **47**, 288–298.
20. Morishita,K., Parker,D., Mucenski,M., Jenkins,N., Copeland,N. and Ihle,J. (1988) Retroviral activation of a novel gene encoding a zinc finger protein in IL-3-dependent myeloid leukemia cell lines. *Cell*, **54**, 831–840.
21. Du,Y., Jenkins,N. and Copeland,N. (2005) Insertional mutagenesis identifies genes that promote the immortalization of primary bone marrow progenitor cells. *Blood*, **106**, 3932–3939.
22. Arai,S., Yoshimi,A., Shimabe,M., Ichikawa,M., Nakagawa,M., Imai,Y., Goyama,S. and Kurokawa,M. (2011) Evi-1 is a transcriptional target of mixed-lineage leukemia oncoproteins in hematopoietic stem cells. *Blood*, **117**, 6304–6314.
23. Nishikata,I., Sasaki,H., Iga,M., Tateno,Y., Imayoshi,S., Asou,N., Nakamura,T. and Morishita,K. (2003) A novel EVI1 gene family, MEL1, lacking a PR domain (MEL1S) is expressed mainly in t(1;3)(p36;q21)-positive AML and blocks G-CSF-induced myeloid differentiation. *Blood*, **102**, 3323–3332.
24. Yamato,G., Yamaguchi,H., Handa,H., Shiba,N., Kawamura,M., Wakita,S., Inokuchi,K., Hara,Y., Ohki,K., Okubo,J. *et al.* (2017) Clinical features and prognostic impact of PRDM16 expression in adult acute myeloid leukemia. *Genes Chromosomes Cancer*, **56**, 800–809.
25. Zhou,B., Wang,J., Lee,S., Xiong,J., Bhanu,N., Guo,Q., Ma,P., Sun,Y., Rao,R., Garcia,B. *et al.* (2016) PRDM16 Suppresses MLL1r leukemia via intrinsic histone methyltransferase activity. *Mol. Cell*, **62**, 222–236.
26. Pinheiro,I., Margueron,R., Shukeir,N., Eisold,M., Fritzsch,C., Richter,F., Mittler,G., Genoud,C., Goyama,S., Kurokawa,M. *et al.* (2012) Prdm3 and Prdm16 are H3K9me1 methyltransferases required for mammalian heterochromatin integrity. *Cell*, **150**, 948–960.
27. Hanotel,J., Bessodes,N., Thélie,A., Hedderich,M., Parain,K., Van Driessche,B., Brandão Kde,O., Kricha,S., Jorgensen,M., Grapin-Botton,A. *et al.* (2014) The Prdm13 histone methyltransferase encoding gene is a Ptf1a-Rbpj downstream target that suppresses glutamatergic and promotes GABAergic neuronal fate in the dorsal neural tube. *Dev. Biol.*, **386**, 340–357.
28. Koh-Stenta,X., Joy,J., Poulsen,A., Li,R., Tan,Y., Shim,Y., Min,J., Wu,L., Ngo,A., Peng,J. *et al.* (2014) Characterization of the histone methyltransferase PRDM9 using biochemical, biophysical and chemical biology techniques. *Biochem. J.*, **461**, 323–334.
29. Blazer,L., Lima-Fernandes,E., Gibson,E., Eram,M., Loppnau,P., Arrowsmith,C., Schapira,M. and Vedadi,M. (2016) PR Domain-containing protein 7 (PRDM7) is a histone 3 lysine 4 trimethyltransferase. *J. Biol. Chem.*, **291**, 13509–13519.
30. Delwel,R., Funabiki,T., Kreider,B., Morishita,K. and Ihle,J. (1993) Four of the seven zinc fingers of the Evi-1 myeloid-transforming gene are required for sequence-specific binding to GA(C/T)AAGA(T/C)AAGATAA. *Mol. Cell. Biol.*, **13**, 4291–4300.
31. Funabiki,T., Kreider,B. and Ihle,J. (1994) The carboxyl domain of zinc fingers of the Evi-1 myeloid transforming gene binds a consensus sequence of GAAGATGAG. *Oncogene*, **9**, 1575–1581.

32. Bard-Chapeau,E., Jeyakani,J., Kok,C., Muller,J., Chua,B., Gunaratne,J., Batagov,A., Jenjaroenpun,P., Kuznetsov,V., Wei,C. *et al.* (2012) Ecotopic viral integration site 1 (EVI1) regulates multiple cellular processes important for cancer and is a synergistic partner for FOS protein in invasive tumors. *Proc. Natl. Acad. Sci. U.S.A.*, **109**, 2168–2173.
33. Glass,C., Wuertzer,C., Cui,X., Bi,Y., Davuluri,R., Xiao,Y., Wilson,M., Owens,K., Zhang,Y. and Perkins,A. (2013) Global Identification of EVI1 Target Genes in Acute Myeloid Leukemia. *PLoS One*, **8**, e67134.
34. Izutsu,K., Kurokawa,M., Imai,Y., Maki,K., Mitani,K. and Hirai,H. (2001) The corepressor CtBP interacts with Evi-1 to repress transforming growth factor beta signaling. *Blood*, **97**, 2815–2822.
35. Kajimura,S., Seale,P., Tomaru,T., Erdjument-Bromage,H., Cooper,M., Ruas,J., Chin,S., Tempst,P., Lazar,M. and Spiegelman,B. (2008) Regulation of the brown and white fat gene programs through a PRDM16/CtBP transcriptional complex. *Genes Dev.*, **22**, 1397–1409.
36. Nitta,E., Izutsu,K., Yamaguchi,Y., Imai,Y., Ogawa,S., Chiba,S., Kurokawa,M. and Hirai,H. (2005) Oligomerization of Evi-1 regulated by the PR domain contributes to recruitment of corepressor CtBP. *Oncogene*, **24**, 6156–6173.
37. Basta,J. and Rauchman,M. (2015) The nucleosome remodeling and deacetylase complex in development and disease. *Trans. Res.*, **165**, 36–47.
38. Torrado,M., Low,J., Silva,A., Schmidberger,J., Sana,M., Sharifi Tabar,M., Isilak,M., Winning,C., Kwong,C., Bedward,M. *et al.* (2017) Refinement of the subunit interaction network within the nucleosome remodelling and deacetylase (NuRD) complex. *FEBS J.*, **284**, 4216–4232.
39. Millard,C., Varma,N., Saleh,A., Morris,K., Watson,P., Bottrill,A., Fairall,L., Smith,C. and Schwabe,J. (2016) The structure of the core NuRD repression complex provides insights into its interaction with chromatin. *Elife*, **5**, e13941.
40. Schmitges,F., Prusty,A., Faty,M., Stützer,A., Lingaraju,G., Aiwazian,J., Sack,R., Hess,D., Li,L., Zhou,S. *et al.* (2011) Histone methylation by PRC2 is inhibited by active chromatin marks. *Mol. Cell*, **42**, 330–341.
41. Lauberth,S. and Rauchman,M. (2006) A conserved 12-amino acid motif in Sall1 recruits the nucleosome remodeling and deacetylase corepressor complex. *J. Biol. Chem.*, **281**, 23922–23921.
42. Lejon,S., Thong,S., Murthy,A., AlQarni,S., Murzina,N., Blobel,G., Laue,E. and Mackay,J. (2011) Insights into association of the NuRD complex with FOG-1 from the crystal structure of an RbAp48·FOG-1 complex. *J. Biol. Chem.*, **286**, 1196–1203.
43. Liu,Z., Li,F., Zhang,B., Li,S., Wu,J. and Shi,Y. (2015) Structural basis of plant homeodomain finger 6 (PHF6) recognition by the retinoblastoma binding protein 4 (RBBP4) component of the nucleosome remodeling and deacetylase (NuRD) complex. *J. Biol. Chem.*, **290**, 6630–6638.
44. Moody,R., Lo,M., Meagher,J., Lin,C., Stevers,N., Tinsley,S., Jung,I., Matvekas,A., Stuckey,J. and Sun,D. (2018) Probing the interaction between the histone methyltransferase/deacetylase subunit RBBP4/7 and the transcription factor BCL11A in epigenetic complexes. *J. Biol. Chem.*, **293**, 2125–2136.
45. Hong,W., Nakazawa,M., Chen,Y., Kori,R., Vakoc,C., Rakowski,C. and Blobel,G. (2005) FOG-1 recruits the NuRD repressor complex to mediate transcriptional repression by GATA-1. *EMBO J.*, **24**, 2367–2378.
46. Bard-Chapeau,E., Gunaratne,J., Kumar,P., Chua,B., Muller,J., Bard,F., Blackstock,W., Copeland,N. and Jenkins,N. (2013) EVI1 oncoprotein interacts with a large and complex network of proteins and integrates signals through protein phosphorylation. *Proc. Natl. Acad. Sci. U.S.A.*, **110**, e2885–e2894.
47. Spensberger,D., Vermeulen,M., Le Guezennec,X., Beekman,R., van Hoven,A., Bindels,E., Stunnenberg,H. and Delwel,R. (2008) Myeloid transforming protein Evi1 interacts with methyl-CpG binding domain protein 3 and inhibits in vitro histone deacetylation by Mbd3/Mi-2/NuRD. *Biochemistry*, **47**, 6418–6426.
48. R Core Team (2014) *R: A Language and Environment for Statistical Computing*. R Foundation for Statistical Computing, Vienna, http://www.R-project.org/.
49. Teo,G., Liu,G., Zhang,J., Nesvizhskii,A., Gingras,A. and Choi,H. (2014) SAINTexpress: improvements and additional features in Significance Analysis of INTeractome software. *J. Proteomics*, **4**, 37–43.
50. Luijsterburg,M., Lindh,M., Acs,K., Vrouwe,M., Pines,A., van Attikum,H., Mullenders,L. and Dantuma,N. (2012) DDB2 promotes chromatin decondensation at UV-induced DNA damage. *J. Cell Biol.*, **197**, 267–281.
51. Kabsch,W. (2010) XDS. *Acta Crystallogr. D Biol. Crystallogr.*, **66**, 125–132.
52. Evans,P. and Murshudov,G. (2013) How good are my data and what is the resolution? *Acta Crystallogr. D Biol. Crystallogr.*, **69**, 1204–1214.
53. McCoy,A., Grosse-Kunstleve,R., Adams,P., Winn,M., Storoni,L. and Read,R. (2007) Phaser crystallographic software. *J. Appl. Cryst.*, **40**, 658–674.
54. Murshudov,G., Skubák,P., Lebedev,A., Pannu,N., Steiner,R., Nicholls,R., Winn,M., Long,F. and Vagin,A. (2011) REFMAC5 for the refinement of macromolecular crystal structures. *Acta Crystallogr. D Biol. Crystallogr.*, **67**, 355–367.
55. Emsley,P., Lohkamp,B., Scott,W. and Cowtan,K. (2010) Features and development of Coot. *Acta Crystallogr. D Biol. Crystallogr.*, **66**, 486–501.
56. Baker,N., Sept,D., Joseph,S., Holst,M. and McCammon,J. (2001) Electrostatics of nanosystems: application to microtubules and the ribosome. *Proc. Natl. Acad. Sci. U.S.A.*, **98**, 10037–10041.
57. Abagyan,R., Totrov,M. and Kuznetsov,D. (1994) ICM - a new method for protein modeling and design. Applications to docking and structure prediction from the distorted native conformation. *J. Comp. Chem.*, **15**, 488–506.
58. Pasqualucci,L., Compagno,M., Houldsworth,J., Monti,S., Grunn,A., Nandula,S., Aster,J., Murty,V., Shipp,M. and Dalla-Favera,R. (2006) Inactivation of the PRDM1/BLIMP1 gene in diffuse large B cell lymphoma. *J. Exp. Med.*, **203**, 331–337.
59. He,L., Yu,J., Liu,L., Buyse,I., Wang,M., Yang,Q., Nakagawara,A., Brodeur,G., Shi,Y. and Huang,S. (1998) RIZ1, but not the alternative RIZ2 product of the same gene, is underexpressed in breast cancer, and forced RIZ1 expression causes G2-M cell cycle arrest and/or apoptosis. *Cancer Res.*, **58**, 4238–4244.
60. Deng,Q. and Huang,S. (2004) PRDM5 is silenced in human cancers and has growth suppressive activities. *Oncogene*, **23**, 4903–4910.
61. Zhu,S., Xu,Y., Song,M., Chen,G., Wang,H., Zhao,Y., Wang,Z. and Li,F. (2016) PRDM16 is associated with evasion of apoptosis by prostatic cancer cells according to RNA interference screening. *Mol. Med. Rep.*, **14**, 3357–3361.
62. Goyama,S., Nitta,E., Yoshino,T., Kako,S., Watanabe-Okochi,N., Shimabe,M., Imai,Y., Takahashi,K. and Kurokawa,M. (2010) EVI-1 interacts with histone methyltransferases SUV39H1 and G9a for transcriptional repression and bone marrow immortalization. *Leukemia.*, **24**, 81–88.
63. Lai,A. and Wade,P. (2011) Cancer biology and NuRD: a multifaceted chromatin remodelling complex. *Nat. Rev. Cancer*, **11**, 588–596.
64. Fu,J., Qin,L., He,T., Qin,J., Hong,J., Wong,J., Liao,L. and Xu,J. (2011) The TWIST/Mi2/NuRD protein complex and its essential role in cancer metastasis. *Cell Res.*, **21**, 275–289.
65. Srinivasan,R., Mager,G., Ward,R., Mayer,J. and Svaren,J. (2006) NAB2 represses transcription by interacting with the CHD4 subunit of the nucleosome remodeling and deacetylase (NuRD) complex. *J. Biol. Chem.*, **281**, 15129–15137.
66. Aguilera,C., Nakagawa,K., Sancho,R., Chakraborty,A., Hendrich,B. and Behrens,A. (2011) c-Jun N-terminal phosphorylation antagonises recruitment of the Mbd3/NuRD repressor complex. *Nature*, **469**, 231–235.
67. Reynolds,N., Salmon-Divon,M., Dvinge,H., Hynes-Allen,A., Balasooriya,G., Leaford,D., Behrens,A., Bertone,P. and Hendrich,B. (2012) NuRD-mediated deacetylation of H3K27 facilitates recruitment of Polycomb Repressive Complex 2 to direct gene repression. *EMBO J.*, **31**, 593–605.
68. Zhao,S., Choi,M., Overton,J., Bellone,S., Roque,D., Cocco,E., Guzzo,F., English,D., Varughese,J., Gasparrini,S. *et al.* (2013) Landscape of somatic single-nucleotide and copy-number mutations in uterine serous carcinoma. *Proc. Natl. Acad. Sci. U.S.A.*, **19**, 2916–2921.